Research Article

Nano Research
2023, 16(5): 6870–6880

ISSN 1998-0124 CN 11-5974/O4
https://doi.org/10.1007/s12274-023-5409-4

FeCo alloy/N, S co-doped carbon aerogel derived from directional-casting cellulose nanofibers for rechargeable liquid flow and flexible Zn–air batteries

Yiwen Zhang[1,§], Xifeng Zhang[1,§], Yuting Li[1], Juan Wang[1] (✉), Sibudjing Kawi[2] (✉), and Qin Zhong[1] (✉)

[1] *School of Chemistry and Chemical Engineering, Nanjing University of Science and Technology, Nanjing 210094, China*
[2] *Department of Chemical and Biomolecular Engineering, National University of Singapore, Singapore 117582, Singapore*
[§] *Yiwen Zhang and Xifeng Zhang contributed equally to this work.*

Received: 16 October 2022 / **Revised:** 10 December 2022 / **Accepted:** 13 December 2022

ABSTRACT

Bifunctional oxygen reduction reaction (ORR) and oxygen evolution reaction (OER) electrocatalysts with the advantages of excellent activity and stability are the vital components of air cathodes for rechargeable Zn–air batteries (ZABs). Herein, the carbon aerogel with honeycomb-like structure, N and S double doping and loaded with FeCo alloy nanoparticles (NSCA/FeCo) was prepared successfully as cathodes for rechargeable liquid flow and two-dimensional flexible ZABs by clever directional casting. The interaction between the bimetallic alloy and the double-doped carbon with specifical structure, large surface, and great conductivity endows NSCA/FeCo with effective ORR/OER active sites and small charge/mass transport barrier, thus achieving outstanding bifunctional catalytic performance. The NSCA/FeCo displays a half-wave potential of +0.85 V (vs. reversible hydrogen electrode (RHE)) for ORR and an overpotential of 335 mV at a current density of 10 mA·cm^{-2} for OER, which is even comparable to the performance of noble-metal catalysts in relevant fields (Pt/C for ORR and RuO_2 for OER). Consequently, the rechargeable liquid flow ZABs assembled with NSCA/FeCo showed excellent performance (maximum power density: 132.0 mW·cm^{-2}, specific capacity: 804.5 Wh·kg^{-1} at 10 mA·cm^{-2}, charge and discharge cycle stability of more than 250 cycles). Furthermore, the flexible NSCA/FeCo-based ZABs have a maximum power density of 43.0 mW·cm^{-2}, outstanding charging–discharge stability of more than 450 cycles, and exhibit good flexibility under different bending conditions. Therefore, this work has provided an efficient bifunctional electrocatalyst for OER/ORR and a promising strategy of air cathodes for rechargeable and wearable ZABs.

KEYWORDS

carbon aerogel, bifunctional electrocatalyst, FeCo alloy, directional freeze-casting, rechargeable zinc–air batteries, flexible batteries

1 Introduction

With society developing rapidly and the increasing dependence on clean and sustainable next-generation energy sources, propelling the exploration of alternative energy conversion and storage devices has been increasingly important. Rechargeable Zn–air batteries (ZABs), with advantages like high theoretical energy density (1086 Wh·kg^{-1}), inherent safety, and cost-effectiveness, have become a hot topic [1–3]. As a vital component of rechargeable ZABs, air cathode significantly influences the batteries' performance by accelerating oxygen evolution reaction (OER) and oxygen reduction reaction (ORR) which occur during the charge and discharge procedure. Both reactions have intrinsically sluggish kinetics and severely hinder energy conversion, thus employing catalysts to boost reaction process is necessary and pivotal [4–6]. Although, traditional noble metal-based electrocatalysts (e.g., Pt/C for ORR, IrO_2 or RuO_2 for OER) have a degree of catalytic capacity, the challenges of resource scarcity, inferior bifunctional activity, and poor stability limit their application [7–9]. Therefore, designing and developing bifunctional electrocatalysts with high activity, long-term stability, and low cost for ZABs have significant theoretical and practical significance [10, 11].

In the past few years, replacing noble metals with transition metals to achieve sustainable and high-performance battery bifunctional catalysts has become a research hotspot. Among abundant transition metals on earth, Fe and Co are salient and widely used to fabricate electrocatalysts. Some studies have shown that the addition of Fe can adjust the electronic structure of the Co centre and optimize the conductivity of those relative catalysts [12–14]. Particularly, FeCo alloy has shown predominant catalytic activity for ORR, benefiting from the two synergistically providing great active binary centres and electronic valence states [15, 16]. Unfortunately, the unsatisfactory OER catalytic activity of most FeCo alloy catalysts seriously hampers their application in rechargeable ZABs. Combining transition metal with carbon substrate is an effective strategy to break the deadlock. At the same time, since the size and electronegativity of heteroatoms (such as B [17], P [18], N [19], and S [20]) are different from that of C,

Address correspondence to Juan Wang, wangjuan304@njust.edu.cn; Sibudjing Kawi, chekawis@nus.edu.sg; Qin Zhong, zq304@njust.edu.cn

heteroatom-doped carbon materials will undergo structural deformation and charge density change. The defects, active sites, conductivity, wettability, and other properties of carbon materials can be optimized through reasonable regulation of heteroatoms, which makes heteroatom-doped carbon materials widely used in batteries, supercapacitors, ORR electrocatalysts, and other fields [21, 22]. In particular, N and S atoms with strong electronegativity can tailor the charge distribution of adjacent carbon atoms and promote oxygen molecules' adsorption and reduction process. Therefore, the synergistic effect of FeCo alloy and N, S co-doped carbon substrate can further improve OER catalytic activity, resulting in an excellent bifunctional catalytic property [23].

As a candidate for carbon-based precursors and a renewable energy source, biomass (such as chitosan, cellulose, and agarose, etc.) has the preponderance of low cost, abundant resources, and environmental friendliness [24]. Among them, cellulose nanofibers (CNFs) are common and abundant biomass obtained from the primary cell walls of green plants such as wood and cotton. And the oxidized CNF possesses an interconnected network structure, large oxygen-containing functional groups, high metal ion adsorption capacity, and good carbon retention, which contributes to forming various porous carbon-based catalysts as precursor templates [25, 26]. Simultaneously, the morphological design of hierarchical porous carbon materials is also crucial for mass and charge transfer in electrochemical processes. Freeze-casting, a promising technique, can be used to fabricate three-dimensional (3D) porous aerogel with unique microstructure characteristics. Through a simple process of directional growth and freeze-drying sublimation of ice crystals, the unique pore channels can be easily designed [27, 28]. Peng et al. prepared a layered elastic carbon aerogel by the directional freeze-casting of a mixed suspension containing CNF, carbon nanotubes, and graphene oxide [29]. When applied as catalyst support, the customizable 3D aerogel materials have hierarchical porous structures with large specific surface areas to scatter alloy nanoparticles, accelerating the mass transport and exposing more available sites. Based on these considerations, modifying (FeCo alloy and N/S) and customizing (freeze-casting) CNF-derived carbon aerogel is promising as green, cheap, and high-performance electrocatalysts to promote the application of ZABs.

Herein, we present an efficient strategy of combining FeCo alloy with the CNF doped N and S through a process of "oxidation of CNF—freezing casting—carbonization" to prepare a bifunctional electrocatalyst (NSCA/FeCo). The subsequent research indicates that this catalyst has a high surface area and mesoporous structure, resulting in the exposure of more active sites and a higher transport rate of active species. Moreover, the cooperation of alloy nanoparticles and N, S-doped carbon substrate endows NSCA/FeCo excellent OER and ORR catalytic properties with a ΔE of 0.75 V under alkaline condition (0.1 M KOH). After that, we successfully used the NSCA/FeCo to assemble liquid flow ZABs and flexible ZABs and found that they had outstanding performance in the charge and discharge process. NSCA/FeCo-based liquid flow ZABs deliver a performance with a maximum power density of 132.0 $mW \cdot cm^{-2}$, a specific capacity of 804.5 $Wh \cdot kg^{-1}$ at 10 $mA \cdot cm^{-2}$, and charge–discharge cycle stability of more than 250 cycles. The flexible NSCA/FeCo-based ZABs exhibit a maximum power density of 43.0 $mW \cdot cm^{-2}$, charge–discharge stability of more than 450 cycles, and good flexibility under different bending conditions. This work testifies that the bifunctional catalyst NSCA/FeCo with a peculiar 3D structure and plentiful active sites can stimulate the development of rechargeable ZABs.

2 Experimental

2.1 Materials

Ferrous chloride tetrahydrate ($FeCl_2 \cdot 4H_2O$, analytical reagent (AR)), cobalt chloride hexahydrate ($CoCl_2 \cdot 6H_2O$, AR), dicyandiamide, and thiourea were all purchased from Guangdong Guanghua Technology Co., Ltd. Cellulose Suspension (≈ 2 wt.%) was purchased from Guangdong Zhongshan Nanofiber New Material Co., Ltd., China. 5 wt.% Nafion Solution, 20 wt.% Pt/C, and RuO_2 were purchased from Shanghai Hesen Electric Co., Ltd., China. All other reagents were used as received unless otherwise noted.

2.2 Preparation of catalyst

2.2.1 *Preparation of oxidized CNF*

CNFs were oxidized via a modified method with 2,2,6,6-tetramethyl-1-piperidinyloxy (TEMPO) [30]. Firstly, 0.016 g TEMPO and 0.1 g NaBr were dissolved in 100 mL 2 wt.% CNF suspension by magnetic stirring. Then moderate NaClO (5 $mmol \cdot g_{CNF}^{-1}$) was added to form the homogeneous suspension. Afterward, 0.5 M NaOH solution was dropwise added to the above solution to adjust the pH value. When the pH value became 10 and remained stable, the sample was washed by centrifuge with deionized water and ethanol several times, respectively. Finally, the solid was dispersed into ultra-pure water to obtain 1.5 wt.% oxidized CNF suspension by a high-speed homogenizer at 15,000 rpm for 5 min.

2.2.2 *Preparation of NSCA/FeCo*

The mixed solution of 500 mg dicyandiamide, 250 mg thiourea, 25 mg $FeCl_2 \cdot 4H_2O$, 27 mg $CoCl_2 \cdot 6H_2O$, and 20 mL oxidized CNF suspension was stirred at room temperature for 2 h to get a uniform solution. Then the solution was poured into a specific mold (50 mm × 50 mm × 20 mm) and directed frozen using liquid nitrogen, followed by freeze-drying for 48 h to get an aerogel precursor. Finally, the aerogel was pyrolyzed at 900 °C for 2 h under Ar atmosphere with a ramping rate of 5 $°C \cdot min^{-1}$ to fabricate NSCA/FeCo. CA/FeCo, NSCA, and CA were also prepared using the same method without adding dicyandiamide and thiourea, metal-salt, and all of them, respectively.

2.3 Physical characterizations

The crystalline phase of catalysts was measured by X-ray diffraction (XRD) with a Cu Kα radiation source on a Bruker D8 ADVANCE diffractometer. Field-emission scanning electron microscope (FE-SEM, FEI Quanta 250 FEG, America) was used to measure the surface morphology of catalysts. The microstructure of catalysts was further analyzed by high-resolution transmission electron microscopy (HRTEM) on a Tecnai 12 (Philips, Holland) accompanied by elemental mapping. The Brunaure–Emmett–Teller (BET) method and Barrett–Joyner–Halenda (BJH) mode were recorded on ASAP 2460. Raman was carried out on Aramis. X-ray photoelectron spectroscopy (XPS) was collected on a Thermo-VG Scientific Escalab 250 spectrometer.

2.4 Electrochemical characterization

CHI 760E electrochemical workstation and a three-electrode system were used for electrochemical testing. A glassy carbon (GC) rotating disk electrode (RDE, 5 mm in diameter), a Hg/HgO electrode, and a carbon rod were used as the working electrode, reference electrode, and counter electrode, respectively. The electrolyte was 0.1 M KOH solution which was bubbled with oxygen for 30 min before testing. The RDE was polished using

alumina slurry on felt-polished pads, followed by ultrasonic cleaning before preparing the working electrode. 4 mg catalyst power was added to the mixture solution of 300 μL ultra-pure water, 150 μL ethanol, and 50 μL 5 wt.% Nafion solution, which was then ultrasonicated for 30 min to form a homogenous ink. Then 10 μL of the ink was dropped on the RDE prepared and dried at room temperature to get the working electrode with catalyst loading of 0.4 mg·cm^{-2}. Besides, two working electrodes of 20 wt.% Pt/C and RuO_2 were prepared by the same process as contrasts for ORR and OER, respectively. All of the potentials have been converted to the potentials versus reversible hydrogen electrode (RHE) according to the following formula

$$E_{RHE} = E_{Hg/HgO} + 0.098 + 0.059 \times pH \quad (1)$$

A rotating ring disk electrode (RRDE) was used to measure the ORR process's electron-transfer number (n). Linear sweep voltammetry (LSV) curves were obtained at a scan rate of 5 mV·s^{-1} with the rotating speed of 1600 rpm to get the ring current (I_R) and disk current (I_D). The hydrogen peroxide yield (H_2O_2%) and n were calculated with the following equations

$$HO_2^-\% = 200 \times \frac{I_R}{N \times I_D + I_R} \quad (2)$$

$$n = \frac{4I_R}{N \times I_D + I_R} \quad (3)$$

where N is the ring collection efficiency (N is 0.38).

3 Results and discussion

3.1 Physical characterization of catalysts

The fabrication process of FeCo/N, S co-doped carbon aerogel (NSCA/FeCo) is revealed in Fig. 1(a). As a pretreatment, CNFs were oxidized by TEMPO to get the oxidized cellulose nanofibers (OCNFs). OCNFs are ideal scaffolds for constructing 3D ordered porous carbon material network structures, with good water dispersion and abundant oxygen-containing functional groups (e.g., –OH and –COOH), which provide various possibilities for modification [26, 29]. As illustrated in Fig. S1 in the Electronic Supplementary Material (ESM), the Fourier transform infrared

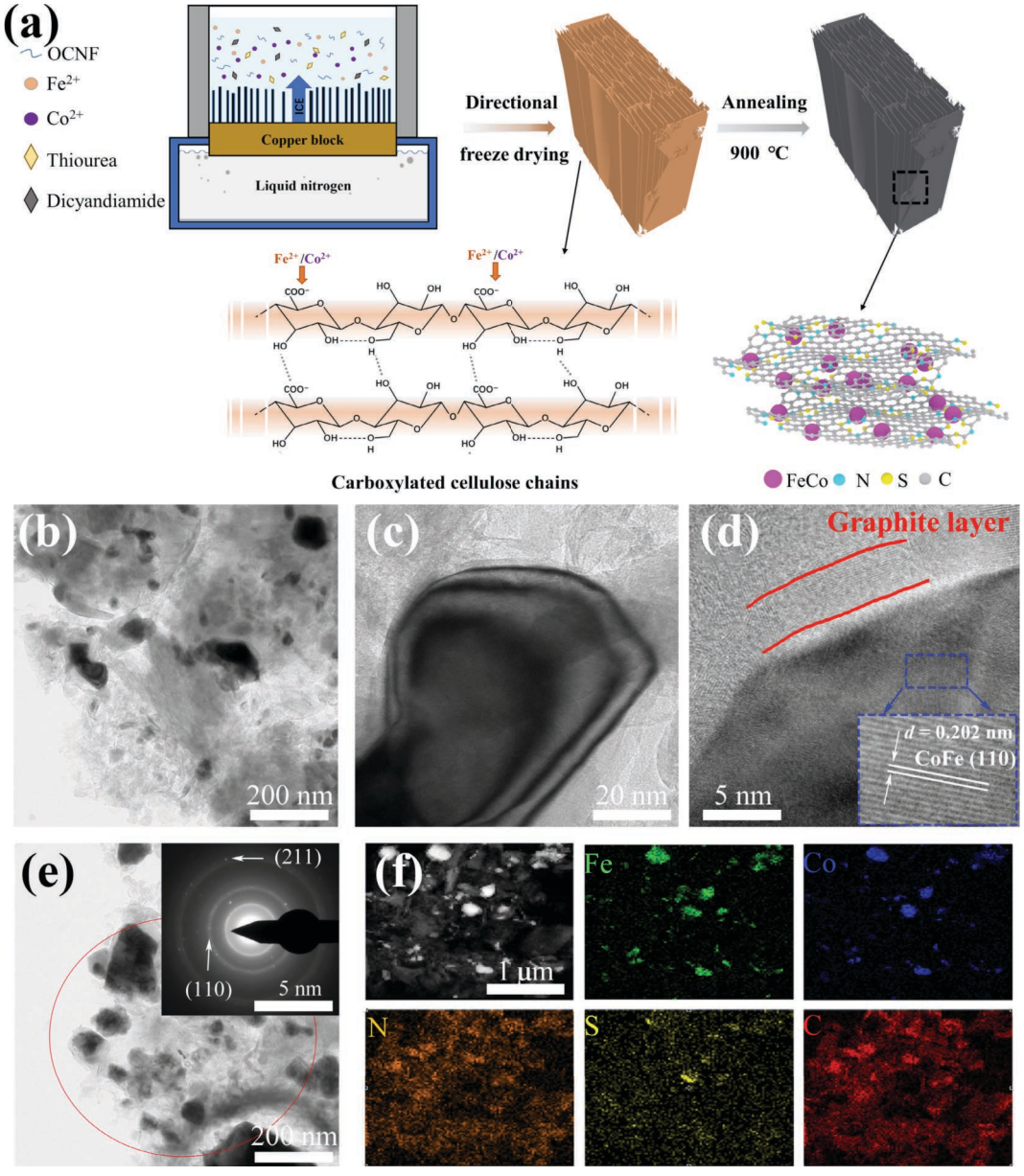

Figure 1 Characterization of NSCA/FeCo. (a) Schematic diagram of the synthesis process, (b) and (c) TEM images at different resolutions (200 and 20 nm), (d) HRTEM image, (e) TEM and corresponding SAED (inset), and (f) high-angle annular dark-field-STEM (HAADF-STEM) images and corresponding element distribution maps.

spectroscopy (FTIR) spectrum of OCNF shows three peaks of hydroxyl (3000–3600 cm^{-1}, O–H), carboxyl (1620 cm^{-1}, C=O), and C–O (1200 cm^{-1}), which confirmed the presence of a large number of oxygen-containing functional groups on OCNF. The abundant carboxylate groups generated on the surface of the nanofibers can act as anchoring sites for strong Lewis acids (such as Fe^{2+} and Co^{2+}). The interaction between them forms stable coordination bonds, thus promoting the uniform dispersion of metal sites in the OCNF network skeleton [31]. Besides, dicyandiamide and thiourea (polymers rich in nitrogen and sulfur) were added to the precursor solution as heteroatomic dopants, which also help to anchor Fe/Co atoms in a highly dispersed manner through strong coordination interactions [32]. With the strategy of directional freezing, as the ice crystals grow vertically in the uniformly dispersed precursor solution, the OCNF and interacting Fe^{2+}/Co^{2+}, dicyandiamide and thiourea form a dense and interconnected network structure under the extrusion of the ice crystals [28, 33, 34]. Finally, NSCA/FeCo was obtained with regular vertical pores and a 3D connected pore structure after freeze-drying and high-temperature pyrolysis.

SEM and TEM measurements investigated the prepared electrocatalysts' surface morphology and structural properties. Figures S2(a) and S2(b) in the ESM present cross-sectional SEM images of NSCA/FeCo. The porous carbon nanosheets are interlinked to form a 3D honeycomb-like resulting from the sublimation of vertically grown ice crystals. In the longitudinal section parallel to the direction of ice crystal growth, many large pores with an average diameter of 16 μm are observed on the carbon sheet, probably originating from the evaporation of H_2O and CO_2 during pyrolysis [35] (Figs. S2(c) and S2(d) in the ESM), which can provide larger accessible sites and contact area with electrolyte or air, thus improving the electrocatalytic performance [36]. Figure S3(a) in the ESM shows the SEM image of NSCA/FeCo at higher resolution, observing the porous carbon aerogel network derived from OCNF during high-temperature annealing. At the same time, metal particles with a diameter of about 40 nm are found on the surface of the aerogel (Fig. S3(b) in the ESM).

The TEM image of NSCA/FeCo in Fig. 1(b) demonstrates that many dispersed metal nanoparticles are uniformly dispersed in the carbon matrix. Importantly, HRTEM image (Fig. 1(c)) clearly reveals that the nanoparticles are fully encapsulated into the heteroatom-doped carbon layer. As seen from the HRTEM image in Fig. 1(d), the lattice spacing of the nanoparticles is 0.202 nm, corresponding to the (110) surface of the FeCo alloy [37]. Under alkaline conditions, the FeCo alloy is coated with a conductive carbon layer, which can efficiently avoid the aggregation and dissolution of the alloy nanoparticles in the complex electrochemical reaction [38]. Additionally, due to the polarization distribution of the electrocatalyst's atomic spin and charge density, the carbon layer doped with N and S can modulate the electronic environment, thus providing effective active sites for ORR and OER [39, 40]. Figure 1(e) demonstrates the pattern of selected area electron diffraction (SAED), and the crystal plane diffraction rings of (110) and (211) of the FeCo alloy are found. In addition, the distributions of Fe, Co, N, S, and C were studied using scanning transmission electron microscope (STEM) and energy dispersive spectroscopy (EDS) (Fig. 1(f) and Fig. S4 in the ESM). It can be seen that Fe and Co mainly exist in the alloy particles, while N and S are mainly doped in the carbon substrate.

The crystal structures of NSCA/FeCo and CA, were described by powder XRD (Fig. 2(a)). The two samples both have wide peaks between 20° and 30°, corresponding to the (002) plane of graphite carbon [41] (PDF#41-1487). In addition, the XRD pattern of NSCA/FeCo shows three characteristic peaks attributed to FeCo (PDF#49-1567), which are located at 44.86° (110), 65.30° (200), and 82.73° (211), respectively [42]. This indicates that FeCo alloy was successfully synthesized in the carbon matrix, while no related N and S species appeared, which is consistent with the HRTEM above results.

To further understand the degree of graphitization defects of different carbon aerogels, Raman tests were conducted on the samples. The Raman spectra are shown in Fig. 2(b). It can be found that there are two wide peaks at 1295 (D peak) and 1560 cm^{-1} (G peak), which are respectively attributed to defective carbon and graphitic carbon [43]. The peak intensity ratios of peak D and peak G (I_D/I_G) of CA, CA/FeCo, and NSCA/FeCo are 0.99, 1.13, and 1.17, respectively. CA has the lowest I_D/I_G value, indicating that it has the highest graphitization degree and good electrical conductivity and can be an ideal conductive carrier of active metal sites [44]. At the same time, it can be determined that with the doping of transition-metal and heteroatoms, more defective carbon is formed in NSCA/FeCo, which is conducive to promoting various electrocatalytic reactions [45].

The specific surface area and pore structure of carbon aerogel were obtained by N_2 isothermal adsorption and desorption measurements. As seen in Fig. 2(c), CA, CA/FeCo, and NSCA/FeCo samples present type IV isotherms of H3 hysteresis loops, indicating the formation of mesoporous structures. The BET analysis illustrates that the specific surface area of NSCA/FeCo was 123.6 $m^2 \cdot g^{-1}$, which is higher than that of CA/FeCo (78.7 $m^2 \cdot g^{-1}$) and CA (78.5 $m^2 \cdot g^{-1}$). The largest specific surface area of NSCA/FeCo may be attributed to the introduction of alloy nanoparticles and heteroatom, which makes the carbon skeleton in NSCA/FeCo produce more pores defects during the catalyst preparation [46]. Besides, the dicyandiamide on the OCNF can form g-C_3N_4 polymer coating during lower annealing temperature and then decompose into gaseous substances at more than 650 °C, which may cause pore expansion too. In addition, the complete graphitization of the sample also means that a large number of oxygen-containing groups are removed and the carbon matrix contracts strongly, thus increasing the porosity of NSCA/FeCo [47]. As demonstrated in Fig. 2(d), the pore size distribution presents that the mesoporous (3–4 nm) account for the largest proportion. This high surface area and mesoporous structure of NSCA/FeCo can effectively maximize the number of exposed active sites and enhance the transport rate of reactive substances, thus significantly improving the ORR/OER activity [48].

XPS spectra were used to analyze the elemental valence states of NSCA/FeCo. As shown in Fig. 3(a), the XPS full spectrum of NSCA/FeCo has five obvious peaks at 169, 285, 399, 532, 711, and 781 eV, which mainly correspond to S 2p (1.16%), C 1s (82.39%), N 1s (4.37%), O 1s (10.83%), Fe 2p (0.61%), and Co 2p (0.64%), respectively. The results mean that Fe, Co, N, and S are successfully doped into the carbon matrix. Figures 3(b)–3(f) present the high-resolution XPS spectra of various elements in NSCA/FeCo. In the Fe 2p spectra (Fig. 3(b)), the peaks are fitted with four components corresponding to Fe^0 (707.7 and 720.8 eV), Fe^{2+} (711.1 and 723.5 eV), Fe^{3+} (714.2 and 727.5 eV), and the satellites peaks (718.7 and 732.7 eV) [49, 50]. The high-resolution Co spectra are also fitted with four components corresponding to Co^0 (779.4 and 795.1 eV), Co^{3+} (781.3 and 796.7 eV), Co^{2+} (786.3 and 802.1 eV), and satellites peaks (788.8 and 807 eV) (Fig. 3(c)) [51]. Fe^0 and Co^0 peaks are attributed to the metals Fe and Co in the FeCo alloy [52, 53]. The related oxidation states (Fe^{3+}/Fe^{2+} and Co^{3+}/Co^{2+}) indicate that partial electrons of metals transfer to heteroatoms (N/S/O) during pyrolysis [54]. Co^{3+} and Fe^{3+} are critical to forming a key intermediate (*OOH) associated with OER activity [43, 55, 56]. Five characteristic peaks of C 1s can be

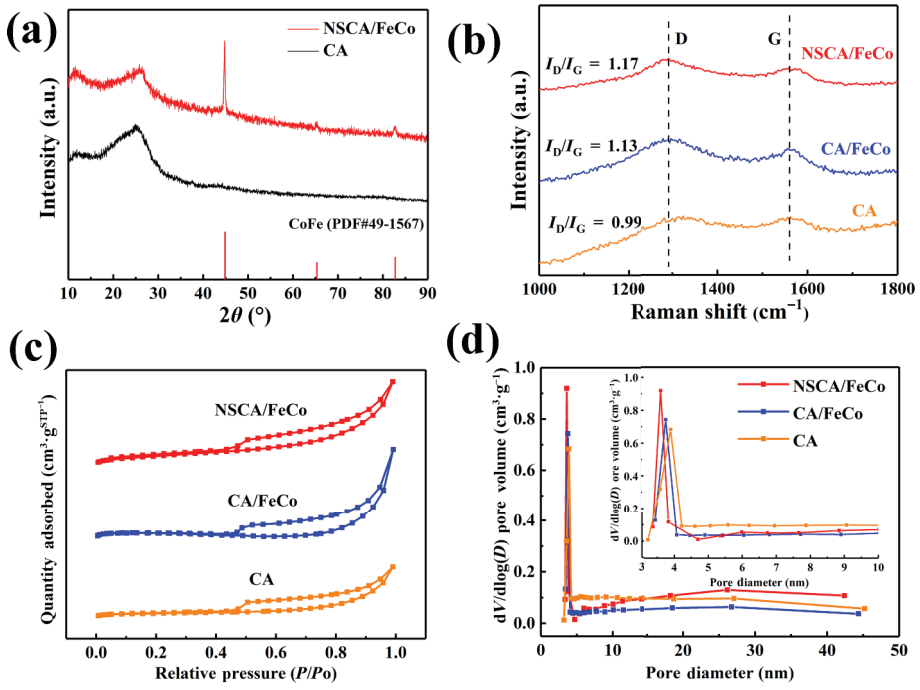

Figure 2 (a) XRD patterns of NSCA/FeCo and CA. (b) Raman spectra, (c) N_2 adsorption–desorption isotherm, and (d) corresponding pore size distribution of NSCA/FeCo, CA/FeCo, and CA.

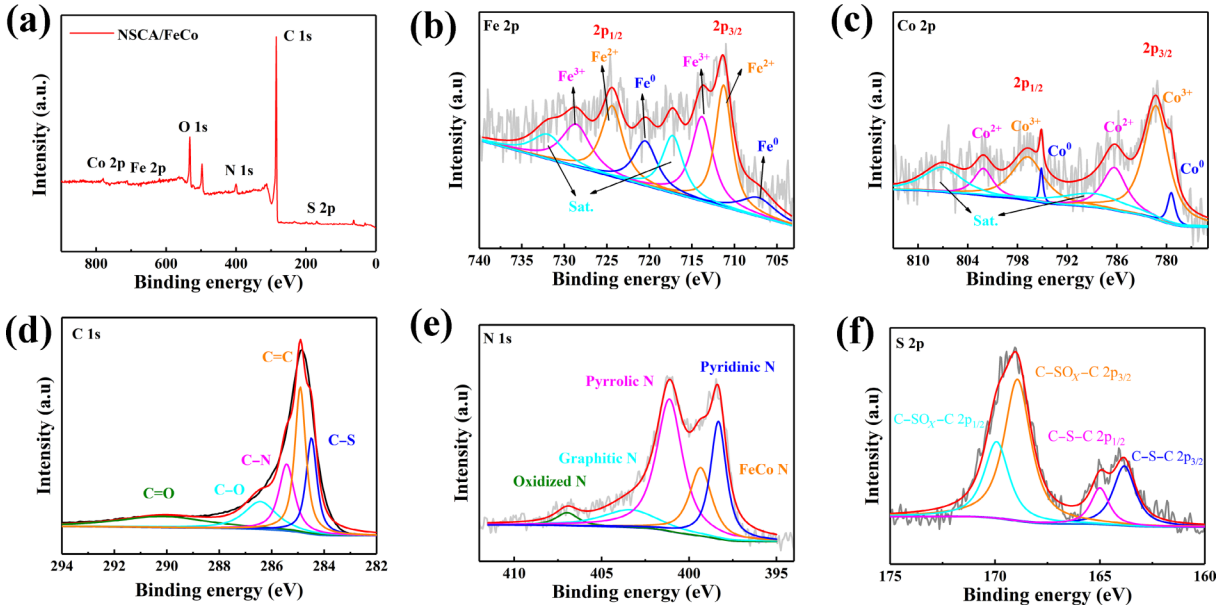

Figure 3 XPS spectra of NSCA/FeCo: (a) full spectrum, (b) Fe 2p, (c) Co 2p, (d) C 1s, (e) N 1s, and (f) S 2p.

discovered in the high-resolution XPS spectra (Fig. 3(d)), which correspond to C=O (290.1 eV), C–O (286.4 eV), C–N (285.4 eV), C=C (284.9 eV), and C–S (284.4 eV), respectively [57]. C–N and C–S bonds imply that N and S atoms have been successfully incorporated into the carbon aerogel. Moreover, C=C and C–O are derived from OCNF precursors, which are generally observed in most biomass carbon substances [58]. As demonstrated in Fig. 3(e), the high-resolution XPS spectra of N 1s have five characteristic peaks at 406.9, 403.3, 401.1, 399.3, and 398.3 eV, which can be attributed to oxidized N, graphitic N, pyrrolic N, transition-metal N, and pyridinic N, respectively [59]. At the same time, the content of different N species was estimated by the integral area under N 1s. As illustrated in Fig. S5 in the ESM, the content of active nitrogen (graphite nitrogen—12.0%, metal nitrogen—20.0%, and pyridine nitrogen—24.5%) accounts for the largest proportion among all kinds of N. It is worth noting that the metal–N is located in the edge exposed region, which is easier to access the reactants and electrolytes than the bulk position as the effective active site of ORR [60]. Therefore, the presence of the N element in the NSCA/FeCo catalyst is of great significance for improving electrochemical performance. As shown in Fig. S6 in the ESM, the O 1s can be fitted in four peaks to C=O (532.06 eV), C–O (533.3 eV), O–S (535.3 eV), and M–O–M (530.1 eV), respectively [23]. It is worth noting that the peak area of M–O is relatively small, which indicates that O is mainly distributed in the carbon layer and exists in the form of C–O/C=O. In addition, C–S–C $2p_{3/2}$ (163.83 eV), C–S–C $2p_{1/2}$ (165 eV), C–SO_x–C $2p_{3/2}$ (168.93 eV), and C–SO_x–C $2p_{1/2}$ (169.92 eV) can be observed in the high-resolution XPS spectra of S 2p (Fig. 3(f)) [61, 62]. These four characteristic peaks correspond to the thiophene sulfur (C–S–C) and sulfur oxide (C–SO_x–C), indicating that S atoms are mainly inserted into the defect sites of carbon. The C–S–C can improve the performance of ORR on account of mismatches between the outermost orbitals of C and neighbouring thiophene-

S atoms [63]. C–SO_x–C indicates that sectional S derived from thiourea reductants is oxidized to sulfate. Furthermore, it is noteworthy that C–SO_x–C is conducive to the adsorption and reduction of oxygen molecules [64].

In conclusion, the M–OOH on the surface of FeCo alloy conduces to enhance the OER catalytic performance [65–67]. Graphitic N, metal N, and pyridinic N, as well as C–SO_x–C and C–S–C, can synergistically enhance the catalytic performance of ORR [62, 68]. These indicate that NSCA/FeCo has great potential as a bifunctional electrocatalyst.

3.2 ORR and OER catalytic performance

RDE evaluated the OER and ORR electrochemical performance of as-prepared catalysts in the electrolyte of 0.1 M KOH, while 20% Pt/C and RuO_2 were also tested under the same condition as a contrast. Figure 4(a) presents the cyclic voltammetry (CV) curves of NSCA/FeCo with a 10 mV·s^{-1} scan rate and manifests the peak of ORR appearing at +0.85 V (vs. RHE) (equivalent to commercial Pt/C). It is better than CA (0.74 V) and CA/FeCo (0.55 V), indicating that NSCA/FeCo has excellent catalytic activity on ORR. This can be further verified by the LSV curves at 1600 rpm (Fig. 4(b)), where the onset potential (E_{onset}) and half-wave potential ($E_{1/2}$) of NSCA/FeCo are +0.97 and +0.820 V, respectively. These are comparable to commercial Pt/C (+0.92 and +0.821 V) and superior to other control samples and recently reported carbon aerogel catalysts (Table S1 in the ESM). Notably, the CA also has significant ORR activity, revealing great ORR catalytic performance of defect sites in the oxygen-containing carbon matrix (O–C). In contrast, CA/FeCo and NSCA/FeCo have elevated ORR performance, suggesting that N, S co-doped carbon (N–C and S–C) and FeCo alloy greatly improved the catalytic activity. The superior ORR electrocatalytic kinetic of NSCA/FeCo was further proved by the small Tafel slope (Pt/C—84 mV·dec^{-1}, CA—151 mV·dec^{-1}, CA/FeCo—156 mV·dec^{-1}, and NSCA/FeCo—89 mV·dec^{-1}) (Fig. 4(c)). The superior ORR activity of NSCA/FeCo could be attributed to the porous structure, high specific surface area, and abundant heteroatomic doping active sites.

Furthermore, to understand the ORR kinetic process of NSCA/FeCo, the electron transfer number and H_2O_2 yield were measured by the RRDE technique. In Fig. 4(d), compared with Pt/C, NSCA/FeCo has an electron transfer number of 3.70–3.85 in the wide potential range from +0.20 to +0.80 V and the yield of H_2O_2 is 7%–14%. This indicates that NSCA/FeCo mainly follows an efficient 4-electron reduction pathway and shows great electrocatalytic selectivity. Besides catalytic activity, stability is also a vital parameter of catalysts in practical applications. We compared the LSV curves before and after the 8000 CV cycles at 100 mV·s^{-1}. As displayed in Figs. 4(e) and 4(f), the $E_{1/2}$ of NSCA/FeCo shifts negatively by 15 mV, while the $E_{1/2}$ of commercial Pt/C decays by 96 mV. The diffusion limiting current density is equivalent to the initial value after the 8000th CV cycle. In conclusion, NSCA/FeCo has great catalytic durability.

After that, the OER activities of the catalysts were also

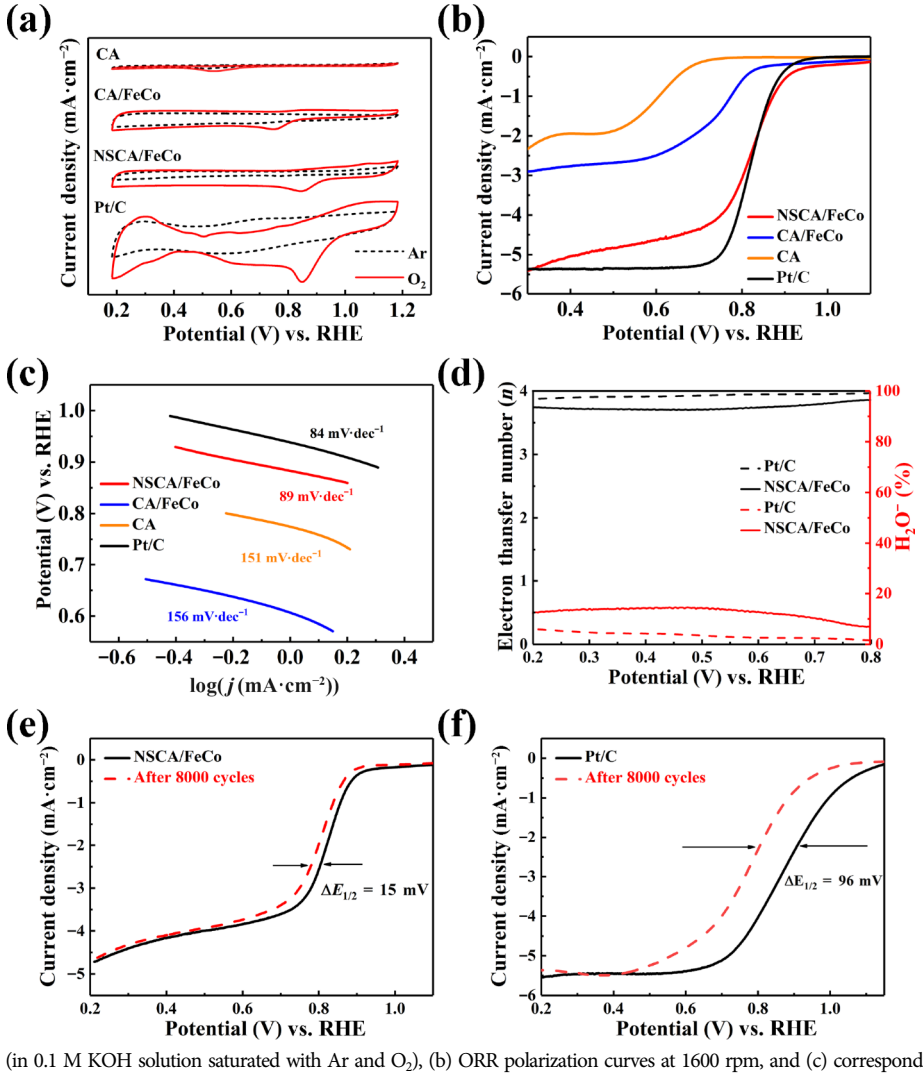

Figure 4 (a) CV curves (in 0.1 M KOH solution saturated with Ar and O_2), (b) ORR polarization curves at 1600 rpm, and (c) corresponding Tafel curves of Pt/C, CA, CA/FeCo, and NSCA/FeCo. (d) RRDE testing of Pt/C and NSCA/FeCo. LSV polarization curves of (e) NSCA/FeCo and (f) Pt/C before and after 8000 CV cycles.

investigated in an O_2-saturated 0.1 M KOH with a speed of 1600 rpm. In Fig. 5(a), the NSCA/FeCo only demands an overpotential of 0.335 V to achieve a current density of 10 mA·cm^{-2}, which is smaller than CA/FeCo (0.487 V), CA and equivalents to RuO_2 (0.332 V). It is noteworthy that the overpotential of NSCA/FeCo is only 0.362 V at the current density of 20 mA·cm^{-2}, which is significantly lower than that of RuO_2 (0.411 V), showing that the catalytic performance of NSCA/FeCo is much better than commercial RuO_2 at high current density. In the meantime, the Tafel slope of NSCA/FeCo (60 mV·dec^{-1}) is the smallest among all samples, implying the fastest OER kinetic of NSCA/FeCo (Fig. 5(b)). As a factor associated with the catalytic activity, electrochemical active surface area (ECSA) is directly proportional to electrochemical double-layer capacitance (C_{dl}) (Figs. S7(b)–S7(d) in the ESM). The C_{dl} of NSCA/FeCo is found to be 20.78 mF·cm^{-2}, which is much high than that for CA (0.65 mF·cm^{-2}) and CA/FeCo (16.47 mF·cm^{-2}) (Fig. S7(a) in the ESM). It further implies that N, S co-doped carbon and FeCo alloys can provide more abundant accessible active sites. The LSV curves of OER normalized by ESCA reveal that the NSCA/FeCo exhibit the best intrinsic activity in all samples (Fig. S8 in the ESM). The current charge transfer processes of the catalysts were researched by electrochemical impedance spectroscopy (EIS). As shown in Fig. 5(c), the Nyquist plots of NSCA/FeCo have a semicircle with a minimum diameter compared to CA/FeCo and CA. The charge transfer resistance (R_{ct}) of NSCA/FeCo is found to be 11.32 Ω, which is smaller than that of CA/FeCo (45.21 Ω) and CA (94.12 Ω), which demonstrates that NSCA/FeCo has an excellent capability for rapid charge transfer during the electrochemical OER process.

Similarly, the OER durability of previous catalysts was also scored via accelerated aging tests: 8000th CV cycles were carried out at a scanning rate of 100 mV·s^{-1} within a voltage range of 1.25–1.75 V (vs. RHE). The NSCA/FeCo shows diminished OER activity, with the potential increasing by 50 mV at 10 mA·cm^{-2} (Fig. 5(d)), moderately larger than the potential change of RuO_2 ($E_{j=10}$ increases by 33 mV) (Fig. 5(e)), due to the continuous erosion of the rich-defect carbon network during long-term electrochemical testing. After the OER durability test, it can be found that the FeCo alloy wrapped in the carbon layer is well protected, but some alloy particles exposed to the edge and surface of the carbon layer undergo a certain oxidation (converted to FeOOH and $Co(OH)_2$), which may be the reason for the increase of OER overpotential (Fig. S9 in the ESM). The bifunctional electrocatalytic activities of catalysts (ORR and OER) are usually estimated by the potential difference between the $E_{1/2}$ and $E_{j=10}$ ($\Delta E = E_{j=10} - E_{1/2}$). As illustrated in Fig. 5(f), the ΔE of NSCA/FeCo is 0.75 V, significantly lower than the ΔE of other comparison samples and Pt/C + RuO_2 (0.85 V), indicating that the NSCA/FeCo has broad application prospects in rechargeable ZABs.

3.3 Rechargeable liquid flow ZABs

Based on the outstanding bifunctional performance of NSCA/FeCo, we assembled the liquid flow ZABs using NSCA/FeCo, zinc flake, and 6 M KOH with 0.2 M $Zn(CH_3COO)_2$ as air cathode, anode, and electrolyte, respectively (Fig. 6(a)). And several electrochemical tests were used to evaluate the possibility of practical application. The standard Pt/C + RuO_2 (weight ratio is 1:1) was prepared for comparison. The NSCA/FeCo-based ZABs have an open circuit voltage (OCV) of 1.49 V, comparable to batteries using commercial Pt/C + RuO_2 (Fig. 6(b)). In Fig. 6(c), the polarization curves of NSCA/FeCo reveal a narrow charge–discharge voltage gap, manifesting that it has a good charge and discharge capacity. In addition, in Fig. 6(d), the peak power density of NSCA/FeCo ZABs is 132 mW·cm^{-2} at a discharge voltage of 0.625 V with a current density of 211 mA·cm^{-2}, which is higher than that of ZABs based on Pt/C + RuO_2 (101.8 mW·cm^{-2} at 0.652 V with 156 mA·cm^{-2}). The constant-current discharge curves of NSCA/FeCo ZABs and Pt/C + RuO_2 at 20 mA·cm^{-2} are shown in Fig. 6(e). The specific capacity of the NSCA/FeCo battery is 804.5 mAh·g_{Zn}^{-1}, which is better than Pt/C + RuO_2 (753.3 mAh·g_{Zn}^{-1}). Correspondingly, the NSCA/FeCo ZABs exhibit an energy density of 973.5 Wh·kg^{-1}, which is also better than the performance of Pt/C + RuO_2 (904.1 Wh·kg^{-1}) (Fig. 6(f)). Excitingly, the ZABs based on NSCA/FeCo catalyst are superior to many bifunctional catalysts based ZABs in the literature (Table S2 in the ESM), further confirming the excellent bifunctional catalytic activity of NSCA/FeCo. Long-term stability is another important factor when applying ZABs in practice and can be measured by a charge–discharge cycling test at 10 mA·cm^{-2}. As seen in Fig. 6(g),

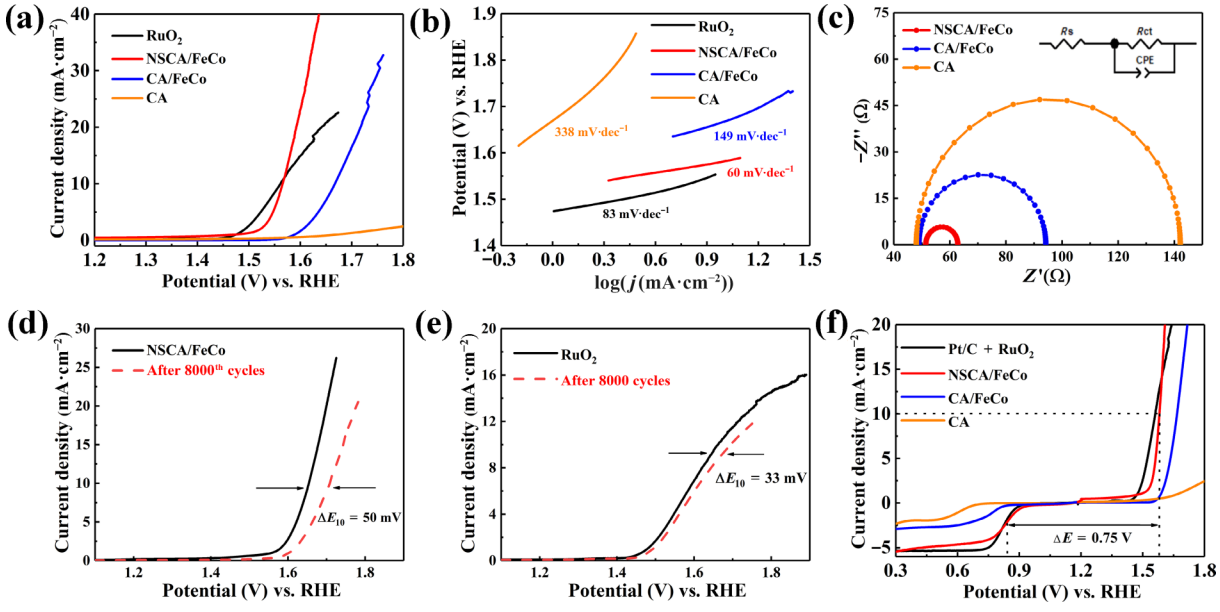

Figure 5 (a) OER for LSV curves with *IR* correction at a scan rate of 10 mV·s^{-1} and (b) corresponding Tafel curves of RuO_2, CA, CA/FeCo, and NSCA/FeCo. (c) Impedance diagrams of CA, CA/FeCo, and NSCA/FeCo. LSV curves of (d) NSCA/FeCo and (e) RuO_2 before and after 8000 cycles of CV scanning. (f) LSV curves of Pt/C + RuO_2, CA, CA/FeCo, and NSCA/FeCo in full ORR + OER potential range.

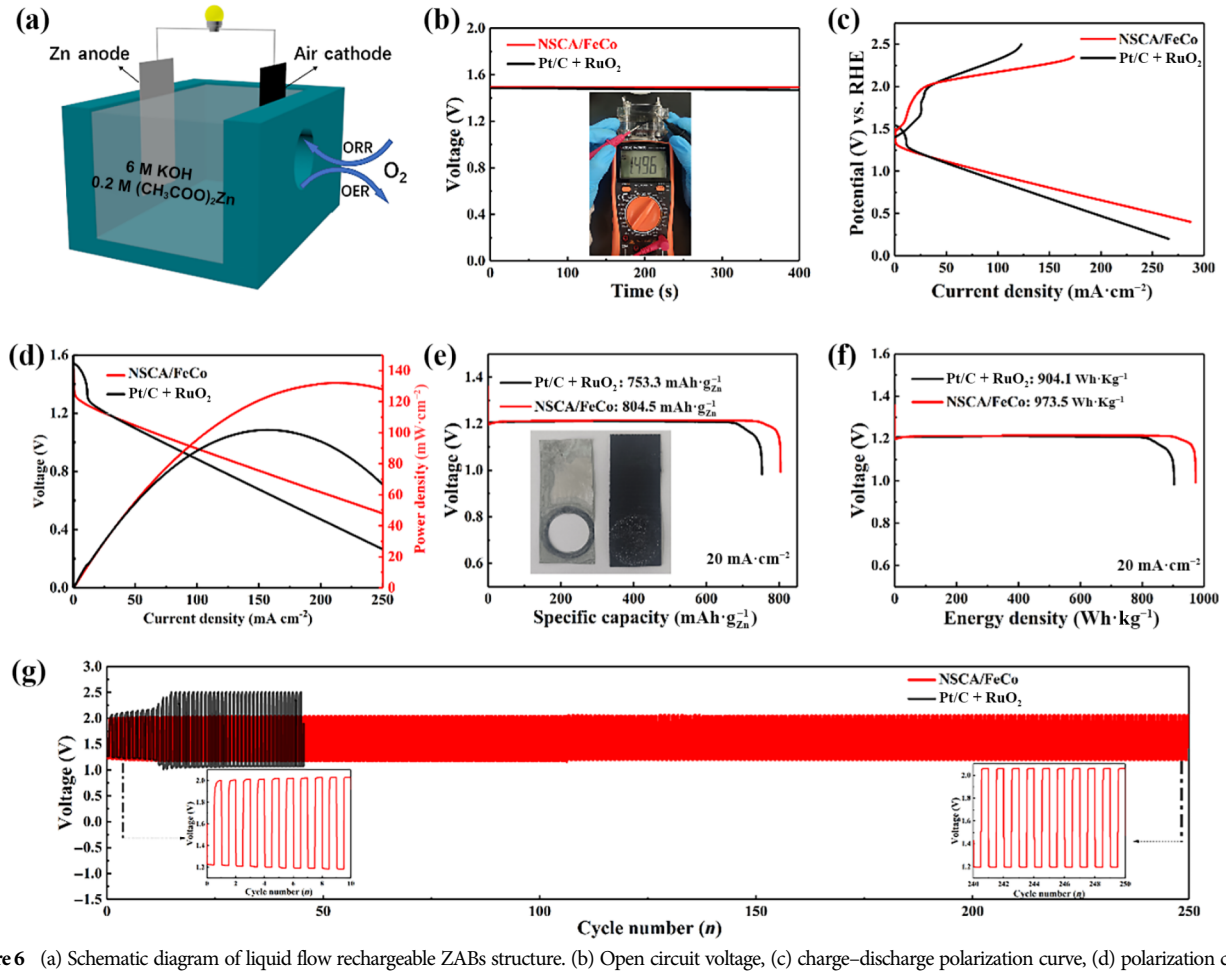

Figure 6 (a) Schematic diagram of liquid flow rechargeable ZABs structure. (b) Open circuit voltage, (c) charge–discharge polarization curve, (d) polarization curves and corresponding power density curves, (e) specific capacity curves, (f) energy density curves, and (g) constant current discharge–charge cycle curve at 10 mA·cm^{-2} of Pt/C + RuO_2 and NSCA/FeCo.

initially, the liquid flow NSCA/FeCo ZABs present a low charge–discharge voltage gap of about 0.82 V, corresponding to a 60% round-trip efficiency, while the Pt/C + RuO_2 ZABs have relatively low round-trip efficiency of 56%. In addition, the NSCA/FeCo ZABs show excellent cycle stability after 250 cycles of consecutive charge–discharge tests while sustaining a round-trip efficiency of 58%. By comparison, the Pt/C + RuO_2 ZABs obviously increase 0.35 V in charge–discharge voltage gap after 20 cycles. These results indicate that NSCA/FeCo catalysts have great application potential in rechargeable ZABs.

3.4 Flexible rechargeable ZABs

The excellent catalytic activity, good stability, and easy operation of NSCA/FeCo prompt it to be assembled into two-dimensional flexible ZABs. Figure 7(a) clearly shows a schematic of assembling flexible ZABs using sodium polyacrylate (PANa) hydrogel instead of KOH solution as a solid electrolyte. In Figs. 7(b) and 7(c), it can be observed that the OCV of the NSCA/FeCo is 1.44 V, and the maximum power density is 43 mW·cm^{-2} (at 64.7 mA·cm^{-2}), which is better than the ZABs based on Pt/C + RuO_2 catalyst (1.38 V, at 39 mW·cm^{-2}). Two flexible NSCA/FeCo ZABs in series can light a LED (3.0 V), demonstrating its potential applications in practical (Fig. 7(d)). Importantly, at 1 mA·cm^{-2}, the round-trip efficiency of the flexible NSCA/FeCo ZABs only decreased from 61.3% to 55.3% after 450 consecutive charge–discharge cycles (Fig. 7(e)). However, the mixed commercial catalyst shows an obvious increase in voltage gap after only 83 charging–discharging cycles. In addition, it can be observed from Fig. 7(f) that the potential gap and round-trip efficiency of ZABs slowly enlarge with the increase of bending degree, indicating that the increase of the bending degree has a certain negative effect on the performance of flexible ZABs. Interestingly, the flexible ZABs can exhibit very stable OCV under different bending angles (inset of Fig. 7(f)).

4 Conclusions

In summary, a bifunctional oxygen catalyst with a 3D honeycomb structure consisting of FeCo alloy and N, S double-doped carbon aerogel (NSCA/FeCo) was prepared by a simple strategy of directional freeze-casting and annealing. The excellent catalytic activity of NSCA/FeCo for ORR and OER was achieved simultaneously by metal–heteroatom–carbon bonding and graphitized carbon-coated alloy particles. At the same time, the catalyst's remarkable conductivity and mesoporous structure contribute to fast mass/charge diffusion, further enhancing the electrocatalytic property under alkaline conditions (ΔE is 0.75 V). Surprisingly, both liquid flow and flexible rechargeable ZABs based on NCSA/FeCo all display high power density, excellent energy density, and cycling stability. Furthermore, the flexible ZABs exhibit wonderful flexibility and stable performance at different bending conditions. Overall, our research work provides an efficient and novel bifunctional electrocatalyst for OER/ORR and a promising strategy for rechargeable ZABs.

Acknowledgements

This work was financially supported by the Fundamental Research Funds for the Central Universities (No. 30920041108).

Electronic Supplementary Material: Supplementary material

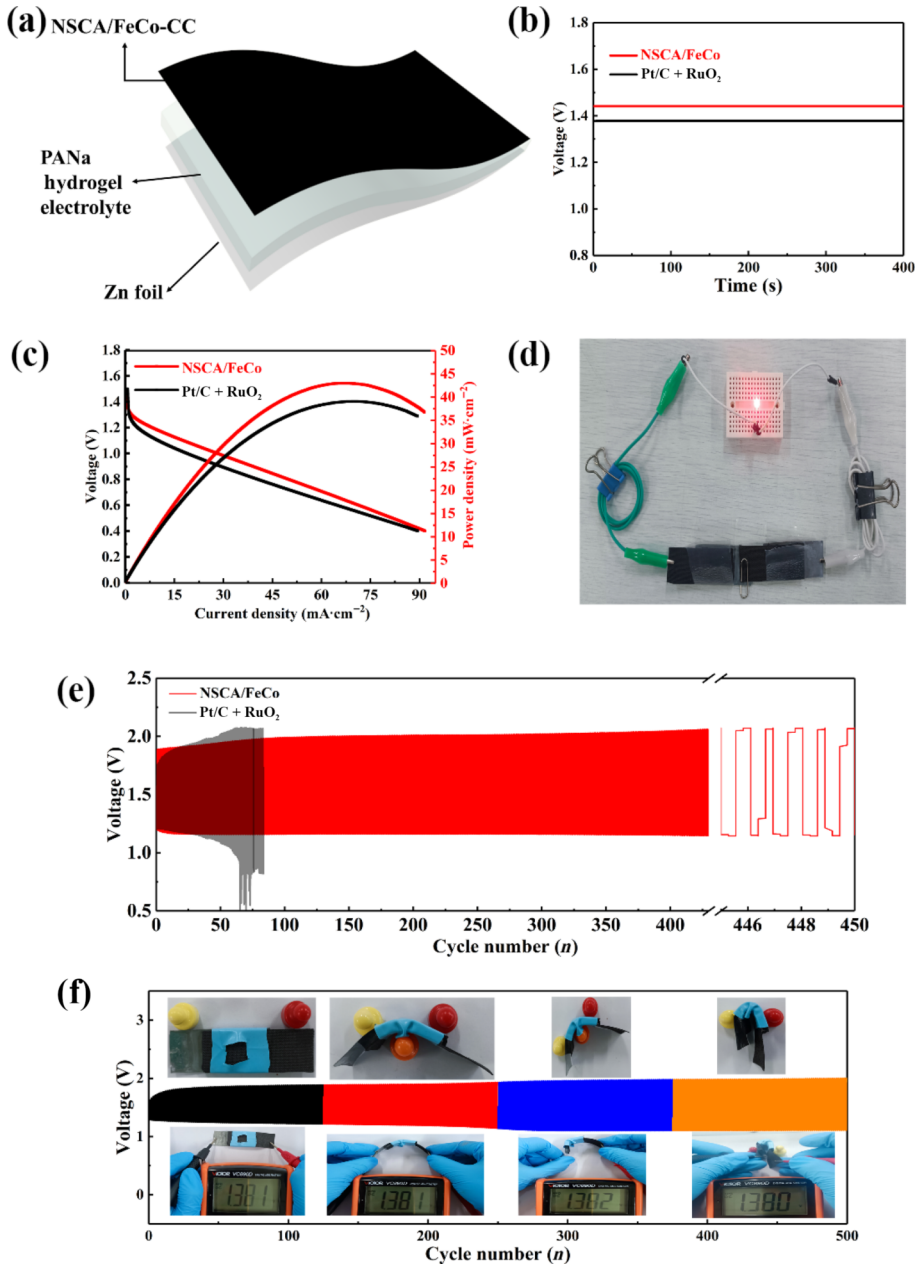

Figure 7 (a) Structure diagram of flexible rechargeable ZABs. (b) Open-circuit voltage test curves and (c) polarization curves and corresponding power density curves of flexible NSCA/FeCo and Pt/C + RuO_2 ZABs. (d) Optical photo of LED (3.0 V) light by two flexible NSCA/FeCo ZABs connected in series. (e) Discharging–charging cycle curves of Pt/C + RuO_2 and NSCA/FeCo at 1 mA·cm^{-2}. (f) Discharging–charging cycle curve at different bending degrees (inset: open circuit voltages at 180°, 120°, 90°, and 0° bending angles and optical photos).

(assembly details of liquid flow rechargeable and flexible ZABs, ZABs performance testing, SEM/TEM images and EDS spectrum of NSCA/FeCo, the summary of various types of N species, XPS spectra of O 1s, CV curves, and comparison with recent reports of similar catalysts) is available in the online version of this article at https://doi.org/10.1007/s12274-023-5409-4.

References

[1] Zhu, Y. T.; Yue, K. H.; Xia, C. F.; Zaman, S.; Yang, H.; Wang, X. Y.; Yan, Y.; Xia, B. Y. Recent advances on MOF derivatives for non-noble metal oxygen electrocatalysts in zinc–air batteries. *Nano-Micro Lett.* **2021**, *13*, 137.

[2] Chen, D.; Chen, X.; Cui, Z. X.; Li, G. F.; Han, B.; Zhang, Q.; Sui, J.; Dong, H. Z.; Yu, J. H.; Yu, L. Y. et al. Dual-active-site hierarchical architecture containing NiFe-LDH and ZIF-derived carbon-based framework composite as efficient bifunctional oxygen electrocatalysts for durable rechargeable Zn–air batteries. *Chem. Eng. J.* **2020**, *399*, 125718.

[3] Fu, J.; Liang, R. L.; Liu, G. H.; Yu, A. P.; Bai, Z. Y.; Yang, L.; Chen, Z. W. Recent progress in electrically rechargeable zinc–air batteries. *Adv. Mater.* **2019**, *31*, 1805230.

[4] Hou, C. C.; Zou, L. L.; Wang, Y.; Xu, Q. MOF-mediated fabrication of a porous 3D superstructure of carbon nanosheets decorated with ultrafine cobalt phosphide nanoparticles for efficient electrocatalysis and zinc–air batteries. *Angew. Chem., Int. Ed.* **2020**, *59*, 21360–21366.

[5] Fu, X. M.; Chen, Y. Y.; Wang, T.; Li, Z. W.; Lei, Y.; Kawi, S. Core-shell nanoarray structured La doped $Cu(OH)_2$@NiCo layered double hydroxide for oxygen evolution reaction. *Int. J. Hydrog. Energy* **2022**, *47*, 27996–28006.

[6] Xu, L.; Wu, S. Q.; He, X. Y.; Wang, H.; Deng, D. J.; Wu, J. C.; Li, H. N. Interface engineering of anti-perovskite Ni_3FeN/VN heterostructure for high-performance rechargeable zinc–air batteries. *Chem. Eng. J.* **2022**, *437*, 135291.

[7] Yin, M. Y.; Zhang, Y. Y.; Bian, Z. F.; Bu, Y. F.; Chen, X. Y.; Zhu, T. L.; Wang, Z. G.; Wang, J.; Kawi, S.; Zhong, Q. Efficient and stable nanoporous functional composited electrocatalyst derived

from Zn/Co-bimetallic zeolitic imidazolate frameworks for oxygen reduction reaction in alkaline media. *Electrochim. Acta* **2019**, *299*, 610–617.

[8] Li, Y. T.; Chen, X. Y.; Wang, J.; Wang, Z. G.; Kawi, S.; Zhong, Q. One-step synthesis of interwoven MoS_2–$CoNi_2S_4$ heterostructures as high-activity water oxidation electrocatalysts. *Catal. Today* **2021**, *364*, 132–139.

[9] Wang, Y. B.; Jiang, Y.; Zhao, Y. X.; Ge, X. L.; Lu, Q.; Zhang, T.; Xie, D. S.; Li, M.; Bu, Y. F. Design strategies of perovskite nanofibers electrocatalysts for water splitting: A mini review. *Chem. Eng. J.* **2023**, *451*, 138710.

[10] Liu, G. H.; Li, J. D.; Fu, J.; Jiang, G. P.; Lui, G.; Luo, D.; Deng, Y. P.; Zhang, J.; Cano, Z. P.; Yu, A. P. et al. An oxygen-vacancy-rich semiconductor-supported bifunctional catalyst for efficient and stable zinc–air batteries. *Adv. Mater.* **2019**, *31*, 1806761.

[11] Wu, S. Q.; Deng, D. J.; Zhang, E. J.; Li, H. N.; Xu, L. CoN nanoparticles anchored on ultra-thin N-doped graphene as the oxygen reduction electrocatalyst for highly stable zinc–air batteries. *Carbon* **2022**, *196*, 347–353.

[12] Wang, Y. Y.; Kumar, A.; Ma, M.; Jia, Y.; Wang, Y.; Zhang, Y.; Zhang, G. X.; Sun, X. M.; Yan, Z. F. Hierarchical peony-like FeCo-NC with conductive network and highly active sites as efficient electrocatalyst for rechargeable Zn–air battery. *Nano Res.* **2020**, *13*, 1090–1099.

[13] Wu, N.; Lei, Y. P.; Wang, Q. C.; Wang, B.; Han, C.; Wang, Y. D. Facile synthesis of FeCo@NC core–shell nanospheres supported on graphene as an efficient bifunctional oxygen electrocatalyst. *Nano Res.* **2017**, *10*, 2332–2343.

[14] Li, C. L.; Wu, M. C.; Liu, R. High-performance bifunctional oxygen electrocatalysts for zinc–air batteries over mesoporous Fe/Co-N-C nanofibers with embedding FeCo alloy nanoparticles. *Appl. Catal. B Environ.* **2019**, *244*, 150–158.

[15] Wang, Y.; Qiao, M. F.; Mamat, X. An advantage combined strategy for preparing bi-functional electrocatalyst in rechargeable zinc-air batteries. *Chem. Eng. J.* **2020**, *402*, 126214.

[16] Zhang, T. R.; Bian, J. J.; Zhu, Y. Q.; Sun, C. W. FeCo nanoparticles encapsulated in N-doped carbon nanotubes coupled with layered double (Co, Fe) hydroxide as an efficient bifunctional catalyst for rechargeable zinc–air batteries. *Small* **2021**, *17*, 2103737.

[17] Qian, Y. H.; Hu, Z. G.; Ge, X. M.; Yang, S. L.; Peng, Y. W.; Kang, Z. X.; Liu, Z. L.; Lee, J. Y.; Zhao, D. A metal-free ORR/OER bifunctional electrocatalyst derived from metal-organic frameworks for rechargeable Zn–air batteries. *Carbon* **2017**, *111*, 641–650.

[18] Yue, S.; Wang, S. S.; Jiao, Q. Z.; Feng, X. T.; Zhan, K.; Dai, Y. Q.; Feng, C. H.; Li, H. S.; Feng, T. Y.; Zhao, Y. Preparation of yolk–shell-structured $Co_xFe_{1-x}P$ with enhanced OER performance. *ChemSusChem* **2019**, *12*, 4461–4470.

[19] Xu, L.; Deng, D. J.; Tian, Y. H.; Li, H. P.; Qian, J. C.; Wu, J. C.; Li, H. N. Dual-active-sites design of CoN_x anchored on zinc-coordinated nitrogen-codoped porous carbon with efficient oxygen catalysis for high-stable rechargeable zinc-air batteries. *Chem. Eng. J.* **2021**, *408*, 127321.

[20] Li, Y. W.; Zhang, W. J.; Li, J.; Ma, H. Y.; Du, H. M.; Li, D. C.; Wang, S. N.; Zhao, J. S.; Dou, J. M.; Xu, L. Q. Fe-MOF-derived efficient ORR/OER bifunctional electrocatalyst for rechargeable zinc–air batteries. *ACS Appl. Mater. Interfaces* **2020**, *12*, 44710–44719.

[21] Deng, D. J.; Qian, J. C.; Liu, X. Z.; Li, H. P.; Su, D.; Li, H. N.; Li, H. M.; Xu, L. Non-covalent interaction of atomically dispersed Cu and Zn pair sites for efficient oxygen reduction reaction. *Adv. Funct. Mater.* **2022**, *32*, 2203471.

[22] Feng, X.; Bai, Y.; Liu, M. Q.; Li, Y.; Yang, H. Y.; Wang, X. R.; Wu, C. Untangling the respective effects of heteroatom-doped carbon materials in batteries, supercapacitors and the ORR to design high performance materials. *Energy Environ. Sci.* **2021**, *14*, 2036–2089.

[23] Li, G. J.; Tang, Y. B.; Fu, T. T.; Xiang, Y.; Xiong, Z. P.; Si, Y. J.; Guo, C. Z.; Jiang, Z. Q. S, N co-doped carbon nanotubes coupled with CoFe nanoparticles as an efficient bifunctional ORR/OER electrocatalyst for rechargeable Zn-air batteries. *Chem. Eng. J.* **2022**, *429*, 132174.

[24] Wang, Z. H.; Shen, D. K.; Wu, C. F.; Gu, S. State-of-the-art on the production and application of carbon nanomaterials from biomass. *Green Chem.* **2018**, *20*, 5031–5057.

[25] Yao, X. L.; Yu, W. J.; Xu, X.; Chen, F.; Fu, Q. Amphiphilic, ultralight, and multifunctional graphene/nanofibrillated cellulose aerogel achieved by cation-induced gelation and chemical reduction. *Nanoscale* **2015**, *7*, 3959–3964.

[26] Xu, T.; Du, H. S.; Liu, H. Y.; Liu, W.; Zhang, X. Y.; Si, C. L.; Liu, P. W.; Zhang, K. Advanced nanocellulose-based composites for flexible functional energy storage devices. *Adv. Mater.* **2021**, *33*, 2101368.

[27] Chen, C.; Zhang, Y.; Zeng, J.; Zhang, F. Q.; Zhou, K. C.; Bowen, C. R.; Zhang, D. Aligned macroporous TiO_2/chitosan/reduced graphene oxide (rGO) composites for photocatalytic applications. *Appl. Surf. Sci.* **2017**, *424*, 170–176.

[28] Pan, Z. Z.; Nishihara, H.; Iwamura, S.; Sekiguchi, T.; Sato, A.; Isogai, A.; Kang, F. Y.; Kyotani, T.; Yang, Q. H. Cellulose nanofiber as a distinct structure-directing agent for xylem-like microhoneycomb monoliths by unidirectional freeze-drying. *ACS Nano* **2016**, *10*, 10689–10697.

[29] Peng, X. W.; Wu, K. Z.; Hu, Y. J.; Zhuo, H.; Chen, Z. L.; Jing, S. S.; Liu, Q. Z.; Liu, C. F.; Zhong, L. X. A mechanically strong and sensitive CNT/rGO-CNF carbon aerogel for piezoresistive sensors. *J. Mater. Chem. A* **2018**, *6*, 23550–23559.

[30] Saito, T.; Kimura, S.; Nishiyama, Y.; Isogai, A. Cellulose nanofibers prepared by TEMPO-mediated oxidation of native cellulose. *Biomacromolecules* **2007**, *8*, 2485–2491.

[31] Zhou, S. Y.; Kong, X. Y.; Zheng, B.; Huo, F. W.; Strømme, M.; Xu, C. Cellulose nanofiber @ conductive metal–organic frameworks for high-performance flexible supercapacitors. *ACS Nano* **2019**, *13*, 9578–9586.

[32] Chen, Y. M.; Wang, H.; Liu, F. S.; Gai, H. J.; Ji, S.; Linkov, V.; Wang, R. F. Hydrophobic 3D Fe/N/S doped graphene network as oxygen electrocatalyst to achieve unique performance of zinc–air battery. *Chem. Eng. J.* **2018**, *353*, 472–480.

[33] Tian, Y.; Estevez, D.; Wei, H. J.; Peng, M. Y.; Zhou, L. P.; Xu, P.; Wu, C.; Yan, M.; Wang, H. A.; Peng, H. X. et al. Chitosan-derived carbon aerogels with multiscale features for efficient microwave absorption. *Chem. Eng. J.* **2021**, *421*, 129781.

[34] Zhang, X. X.; Wang, H. K.; Cai, Z. Y.; Yan, N.; Liu, M. H.; Yu, Y. Highly compressible and hydrophobic anisotropic aerogels for selective oil/organic solvent absorption. *ACS Sustainable Chem. Eng.* **2019**, *7*, 332–340.

[35] Liu, F.; Wang, C. J.; Sui, X.; Riaz, M. A.; Xu, M. Y.; Wei, L.; Chen, Y. Synthesis of graphene materials by electrochemical exfoliation: Recent progress and future potential. *Carbon Energy* **2019**, *1*, 173–199.

[36] Fei, Y.; Liang, M.; Yan, L. W.; Chen, Y.; Zou, H. W. Co/C@cellulose nanofiber aerogel derived from metal–organic frameworks for highly efficient electromagnetic interference shielding. *Chem. Eng. J.* **2020**, *392*, 124815.

[37] Samanta, A.; Raj, C. R. Bifunctional nitrogen-doped hybrid catalyst based on onion-like carbon and graphitic carbon encapsulated transition metal alloy nanostructure for rechargeable zinc–air battery. *J. Power Sources* **2020**, *455*, 227975.

[38] Zhang, H. W.; Zhao, M. Q.; Liu, H. R.; Shi, S. R.; Wang, Z. H.; Zhang, B.; Song, L.; Shang, J. Z.; Yang, Y.; Ma, C. et al. Ultrastable FeCo bifunctional electrocatalyst on Se-doped CNTs for liquid and flexible all-solid-state rechargeable Zn–air batteries. *Nano Lett.* **2021**, *21*, 2255–2264.

[39] Cao, S.; Shang, W. Z.; Li, G. L.; Lu, Z. F.; Wang, X.; Yan, Y.; Hao, C.; Wang, S. L.; Sun, G. Q. Defect-rich and metal-free N, S co-doped 3D interconnected mesoporous carbon material as an advanced electrocatalyst towards oxygen reduction reaction. *Carbon* **2021**, *184*, 127–135.

[40] Lai, C. L.; Gong, M. X.; Zhou, Y. C.; Fang, J. Y.; Huang, L.; Deng, Z. P.; Liu, X. P.; Zhao, T. H.; Lin, R. Q.; Wang, K. L. et al. Sulphur modulated Ni_3FeN supported on N/S co-doped graphene boosts rechargeable/flexible Zn–air battery performance. *Appl. Catal. B Environ.* **2020**, *274*, 119086.

[41] Yao, Z. H.; Li, Y. T.; Chen, D. S.; Zhang, Y. W.; Bao, X. H.; Wang, J.; Zhong, Q. γ-Fe_2O_3 clusters embedded in 1D porous N-doped

carbon matrix as pH-universal electrocatalyst for enhanced oxygen reduction reaction. *Chem. Eng. J.* **2021**, *415*, 129033.

[42] Kim, K.; Min, K.; Go, Y.; Lee, Y.; Shim, S. E.; Lim, D.; Baeck, S. H. FeCo alloy nanoparticles embedded in N-doped carbon supported on highly defective ketjenblack as effective bifunctional electrocatalysts for rechargeable Zn–air batteries. *Appl. Catal. B Environ.* **2022**, *315*, 121501.

[43] Zhang, Y. W.; Li, Y. T.; Yao, Z. H.; Wang, J.; Zhong, Q. Iron-nickel aerogels anchored on GO nanosheets as efficient oxygen evolution reaction catalysts under industrial conditions. *Int. J. Hydrog. Energy* **2022**, *47*, 6996–7004.

[44] Chen, X. D.; Wang, N.; Shen, K.; Xie, Y. K.; Tan, Y. P.; Li, Y. W. MOF-derived isolated Fe atoms implanted in N-doped 3D hierarchical carbon as an efficient ORR electrocatalyst in both alkaline and acidic media. *ACS Appl. Mater. Interfaces* **2019**, *11*, 25976–25985.

[45] Sheng, J.; Zhu, S.; Jia, G. D.; Liu, X.; Li, Y. Carbon nanotube supported bifunctional electrocatalysts containing iron-nitrogen-carbon active sites for zinc–air batteries. *Nano Res.* **2021**, *14*, 4541–4547.

[46] Pang, H. P.; Sun, P. P.; Gong, H. Y.; Zhang, N.; Cao, J. C.; Zhang, R. H.; Luo, M. F.; Li, Y.; Sun, G. L.; Li, Y. G. et al. Wood-derived bimetallic and heteroatomic hierarchically porous carbon aerogel for rechargeable flow Zn-air batteries. *ACS Appl. Mater. Interfaces* **2021**, *13*, 39458–39469.

[47] Bayram, E.; Yilmaz, G.; Mukerjee, S. A solution-based procedure for synthesis of nitrogen doped graphene as an efficient electrocatalyst for oxygen reduction reactions in acidic and alkaline electrolytes. *Appl. Catal. B Environ.* **2016**, *192*, 26–34.

[48] Lei, Z.; Tan, Y. Y.; Zhang, Z. Y.; Wu, W.; Cheng, N. C.; Chen, R. Z.; Mu, S. C.; Sun, X. L. Defects enriched hollow porous Co-N-doped carbons embedded with ultrafine CoFe/Co nanoparticles as bifunctional oxygen electrocatalyst for rechargeable flexible solid zinc–air batteries. *Nano Res.* **2021**, *14*, 868–878.

[49] Zhang, S. L.; Guan, B. Y.; Lou, X. W. Co-Fe alloy/N-doped carbon hollow spheres derived from dual metal–organic frameworks for enhanced electrocatalytic oxygen reduction. *Small* **2019**, *15*, 1805324.

[50] Zhang, R. Z.; He, S. J.; Lu, Y. Z.; Chen, W. Fe, Co, N-functionalized carbon nanotubes *in situ* grown on 3D porous N-doped carbon foams as a noble metal-free catalyst for oxygen reduction. *J. Mater. Chem. A* **2015**, *3*, 3559–3567.

[51] Meng, H. J.; Pei, S. P.; Li, H.; Zhang, Y. M. CoFe/N, S-C featured with graphitic nanoribbons and multiple CoFe nanoparticles as highly stable and efficient electrocatalysts for the oxygen reduction reaction. *ACS Omega* **2021**, *6*, 11059–11067.

[52] Ma, Y. M.; Gan, L.; Li, D.; Gao, Y. Y.; Yang, X. X.; Wang, K.; Lu, S. Y.; Wu, H.; Ding, S. J.; Xiao, C. H. Rational modulation of N, P co-doped carbon nanotubes encapsulating Co_3Fe_7 alloy as bifunctional oxygen electrocatalysts for zinc-air batteries. *J. Power Sources* **2019**, *441*, 227177.

[53] Liu, X.; Wang, L.; Yu, P.; Tian, C. G.; Sun, F. F.; Ma, J. Y.; Li, W.; Fu, H. G. A Stable bifunctional catalyst for rechargeable zinc–air batteries: Iron-cobalt nanoparticles embedded in a nitrogen-doped 3D carbon matrix. *Angew. Chem., Int. Ed.* **2018**, *57*, 16166–16170.

[54] Xu, Q. C.; Jiang, H.; Li, Y. H.; Liang, D.; Hu, Y. J.; Li, C. Z. In-situ enriching active sites on co-doped Fe-Co_4N@N-C nanosheet array as air cathode for flexible rechargeable Zn–air batteries. *Appl. Catal. B Environ.* **2019**, *256*, 117893.

[55] Zhao, X. M.; Liu, X.; Huang, B. Y.; Wang, P.; Pei, Y. Hydroxyl group modification improves the electrocatalytic ORR and OER activity of graphene supported single and bi-metal atomic catalysts (Ni, Co, and Fe). *J. Mater. Chem. A* **2019**, *7*, 24583–24593.

[56] Xiao, H.; Shin, H.; Goddard, W. A. Synergy between Fe and Ni in the optimal performance of (Ni, Fe)OOH catalysts for the oxygen evolution reaction. *Proc. Natl. Acad. Sci. USA* **2018**, *115*, 5872–5877.

[57] Yao, Z. H.; Chen, D. S.; Li, Y. T.; Lyu, Q. Q.; Wang, J.; Zhong, Q. MOF-derived multi-metal embedded N-doped carbon sheets rich in CNTs as efficient bifunctional oxygen electrocatalysts for rechargeable ZABs. *Int. J. Hydrog. Energy* **2022**, *47*, 984–992.

[58] Sun, T.; Wang, J.; Qiu, C. T.; Ling, X.; Tian, B. B.; Chen, W.; Su, C. L. B, N codoped and defect-rich nanocarbon material as a metal-free bifunctional electrocatalyst for oxygen reduction and evolution reactions. *Adv. Sci.* **2018**, *5*, 1800036.

[59] Wu, K. Z.; Zhang, L.; Yuan, Y. F.; Zhong, L. X.; Chen, Z. X.; Chi, X.; Lu, H.; Chen, Z. H.; Zou, R.; Li, T. Z. et al. An iron-decorated carbon aerogel for rechargeable flow and flexible Zn–air batteries. *Adv. Mater.* **2020**, *32*, e2002292.

[60] Niu, Q. J.; Guo, J. X.; Tang, Y. H.; Guo, X. D.; Nie, J.; Ma, G. P. Sandwich-type bimetal–organic frameworks/graphene oxide derived porous nanosheets doped Fe/Co-N active sites for oxygen reduction reaction. *Electrochim. Acta* **2017**, *255*, 72–82.

[61] Liang, H.; Li, C. W.; Chen, T.; Cui, L.; Han, J. R.; Peng, Z.; Liu, J. Q. Facile preparation of three-dimensional $Co_{1-x}S$/sulfur and nitrogen-codoped graphene/carbon foam for highly efficient oxygen reduction reaction. *J. Power Sources* **2018**, *378*, 699–706.

[62] Li, Y.; Zhou, Y. Z.; Zhu, C. Z.; Hu, Y. H.; Gao, S.; Liu, Q. Q.; Cheng, X. N.; Zhang, L. L.; Yang, J.; Lin, Y. H. Porous graphene doped with Fe/N/S and incorporating Fe_3O_4 nanoparticles for efficient oxygen reduction. *Catal. Sci. Technol.* **2018**, *8*, 5325–5333.

[63] Chen, S.; Chen, S.; Zhang, B. H.; Zhang, J. T. Bifunctional oxygen electrocatalysis of N, S-codoped porous carbon with interspersed hollow CoO nanoparticles for rechargeable Zn–air batteries. *ACS Appl. Mater. Interfaces* **2019**, *11*, 16720–16728.

[64] Khandelwal, M.; Chandrasekaran, S.; Hur, S. H.; Chung, J. S. Chemically controlled *in-situ* growth of cobalt oxide microspheres on N, S-co-doped reduced graphene oxide as an efficient electrocatalyst for oxygen reduction reaction. *J. Power Sources* **2018**, *407*, 70–83.

[65] Guo, W. J.; Li, D. D.; Zhong, D. Z.; Chen, S.; Hao, G. Y.; Liu, G.; Li, J. P.; Zhao, Q. Loading FeOOH on $Ni(OH)_2$ hollow nanorods to obtain a three-dimensional sandwich catalyst with strong electron interactions for an efficient oxygen evolution reaction. *Nanoscale* **2020**, *12*, 983–990.

[66] Li, H. X.; Zhou, Q.; Liu, F. Y.; Zhang, W. L.; Tan, Z.; Zhou, H. H.; Huang, Z. Y.; Jiao, S. Q.; Kuang, Y. F. Biomimetic design of ultrathin edge-riched FeOOH@carbon nanotubes as high-efficiency electrocatalysts for water splitting. *Appl. Catal. B Environ.* **2019**, *255*, 117755.

[67] Wang, Y. B.; Lu, Q.; Ge, X. L.; Li, F.; Chen, L.; Zhang, Z. H.; Fu, Z. P.; Lu, Y. L.; Song, Y.; Bu, Y. F. Molecular-level proton acceptor boosts oxygen evolution catalysis to enable efficient industrial-scale water splitting. *Green Energy Environ.*, in press, DOI: 10.1016/j.gee.2022.07.001.

[68] Li, J. J.; Zhang, Y. M.; Zhang, X. H.; Huang, J. Z.; Han, J. C.; Zhang, Z. H.; Han, X. J.; Xu, P.; Song, B. S, N dual-doped graphene-like carbon nanosheets as efficient oxygen reduction reaction electrocatalysts. *ACS Appl. Mater. Interfaces* **2017**, *9*, 398–405.